Distributed Multipole Model for Design of Permanent-Magnet-Based Actuators

Kok-Meng Lee, *Fellow, IEEE*, and Hungsun Son

George W. Woodruff School of Mechanical Engineering, Georgia Institute of Technology, Atlanta, GA 30332-0405 USA

This paper presents a general method for deriving a closed-form solution for precise calculation of the magnetic field around a permanent magnet (PM) or an electromagnet (EM). The method, referred here as distributed multipole (DMP) modeling, inherits many advantages of the dipole model originally conceptualized in the context of physics, but provides an effective means to account for the shape and magnetization of the physical magnet. Three examples are given to illustrate the procedure of developing a DMP model, which derives an appropriate set of distributed dipoles from a limited set of known field points, for a general cylindrical PM, a customized PM, and a multilayer coil. The DMP modeling method has been validated by comparing simulated fields and calculated forces against data obtained experimentally and numerically; the comparisons show excellent agreement. Finally, we illustrate how the closed-form DMP models can offer an inexpensive means to visualize the effect of the EM fields on the leakage and unexpected flux paths, which have significant influences on the magnetic torque of a spherical motor.

Index Terms—**Actuator design, closed-form solution, dipole, Lorentz force, magnetic field, Maxwell stress tensor, pole shape.**

I. Introduction

THE growing applications of robotics, automation, and mechatronics in nontraditional industries (agricultural, food-processing, and surgical robotics), along with the wide availability of high-coercive rare-earth permanent magnets (PMs) at low cost, have motivated researchers to develop application-oriented PM-based actuators capable of multiple degrees of freedom (DOF) in a single joint [1]–[5]. The interest to have a better understanding of the magnetic fields involved in the direct-drive multi-DOF PM-based actuator has led us to develop a new modeling method to derive closed-form solutions for efficient design and accurate motion control of the actuator.

Existing techniques for analyzing electromagnetic fields of a multi-DOF (position and/or orientation) PM-based actuator rely primarily on three approaches; namely, analytic solutions to Laplace equation, numerical methods, and lumped-parameter analyses with some forms of equivalent circuits. The possibility of obtaining an analytic solution is often remote for devices with complex geometry. Perturbation theory and linear superposition can sometimes render a difficult problem solvable. However, even if an analytic solution is achievable, it often results in a series of space harmonics of nonelementary functions [3], [4] which must be computed if a numeric solution to the problem is desired. Numerical methods (such as the finite-element method) offer a good prediction of the magnetic field for accurate computation of the magnetic torque [5]. However, demanding computational time limits these numerical methods to off-line computation. Most of the real-time computations for optimization and motion control of electromagnetic actuators have relied on lumped parameter approaches to obtain a closed-form solution which generally yields only first-order accuracy. These approaches have difficulties in achieving both accuracy and low computation time simultaneously.

An alternative method has been based on the concept of a magnetic dipole (originally suggested by Fitz Gerlad in 1883) as a tool to characterize potential fields. While the dipole model has been widely used to analyze the magnetic field at a sufficiently large distance for applications [6]–[8] such as electromagnetic wave propagation (antenna dynamics) and geomagnetism (earth polarization), it generally gives a poor approximation when the length scale of the field is very small. For reasons including compact formulation/solutions and intuitive magnetic fields, many researchers (for example, [9] and [10]) continue to develop dipole models for analyzing actuator designs involving permanent magnets. Nedelcu *et al.* [9] used a magnetic dipole model to describe the field of a PM-based device, where each PM is modeled as a doublet. While the model in [9] provides a concise computational formula for the field and the energy flow, it has difficulties in obtaining an accurate magnetic field. De Visschere [10] later pointed out a number of mistakes when comparing the dipole approximation [9] against an analytical 2-D magnetic field solution of a permanent magnet. The existing single dipole model, which is based on the mathematical theory of a doublet, is often studied in the context of physics and valid only for needle-like magnets; thus, it has very limited applications in modern actuator designs.

The paper presents a field modeling method utilizing an assembly of appropriately distributed dipoles to account for the shape and magnetization of the physical magnet. The remainder of this paper offers the following.

1) We provide a relatively complete formulation for deriving the closed-form solution to characterize the magnetic field around a PM or an EM. This method uses a limited set of known field points to construct a distributed multipole (DMP) model for the magnet. The simplicity (and yet precise calculation of the magnetic field) of the closed form solution offers an advantage for real-time applications.
2) Three examples are given to illustrate the procedure of developing a DMP model; a cylindrical PM, a multilayer cylindrical EM, and a customized PM. The models are

Digital Object Identifier 10.1109/TMAG.2007.904709

Color versions of one or more of the figures in this paper are available online at http://ieeexplore.ieee.org.

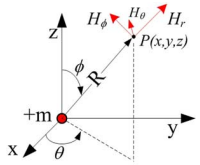

Fig. 1. Field intensity of a source m in spherical coordinates.

validated by comparing simulated fields against known solutions whenever possible, and/or published numerical and experimental results. The comparisons show excellent agreement.

3) Three different methods for calculating magnetic forces using DMP models are compared. The first and second methods calculate the Lorentz force exerted on the current-carrying conductors of the multilayer EM and its equivalent single-layer EM, respectively. The third method treats the EM as a PM and uses the Maxwell stress tensor to obtain the total force acting on the given field. We also demonstrate the use of DMP models to study the effect of different pole shapes on the fields of a spherical motor.

II. Distributed Multipole (DMP) Model

The magnetic field intensity $\mathbf{H}$ of a source $+\mathrm{m}$ (or a sink $-\mathrm{m}$) can be expressed [8] in spherical coordinates (R,θ,ϕ) defined in Fig. 1 as

$$H_r=\frac{(-1)^j}{4\pi R^2}\left[m(t-R/c)+\frac{R}{c}\frac{\partial m(t-R/c)}{\partial t}\right];\ H_\theta=H_\phi=0 \tag{1}$$

where c is the speed of light; m is the strength of the pole; and j takes the value 0 or 1 designating that the pole is a source or a sink, respectively.

We consider here PM-based actuator applications where the order of the length scale is relatively small and consequently R/c is several orders smaller than that of the actuator characteristic time. In addition, the field is continuous and irrotational; and the medium is homogeneous. The irrotational field $(\nabla\times\mathbf{B}=0)$ enables us to define a scalar magnetic potential Φ such that

$$\mathbf{H}=-\nabla\Phi \tag{2a}$$

and

$$\mathbf{B}=\mu_0\mathbf{H} \tag{2b}$$

where μ_0 is the permeability of free space. Since the field is continuous $(\nabla\cdot\mathbf{B}=0)$ and μ_0 is a constant, we have

$$\nabla^2\Phi(\mathbf{R},t)=0. \tag{3}$$

The solution to Laplace's equation (3), which satisfies the field $\mathbf{H}$ in (1) for a source or a sink, is given by

$$\Phi=\frac{(-1)^{j+1}}{4\pi R}m(t). \tag{4}$$

Equation (4) has been used to derive approximate flux paths of a magnet. Two models (pole and doublet) were suggested in [6]. The *pole model* uses a source-and-sink pair at the ends of the magnet. However, as the fields of a physical magnet are everywhere finite, the poles (source and sink) attached at the end of the magnet are singularities (or infinite field density) resulting in significant errors. This is particularly critical at the air gap that is often very small compared to other dimensions. The *doublet model* uses a single dipole at the origin of the magnet and, thus, the magnetic fields outside of the physical magnet being approximated are generally finite. However, the doublet model (much like the pole model) cannot account for the effects of the shape and property of the magnet. An alternative method is to use multiple dipoles to account for the shape of the physical magnet. This method is based on the fact that the Laplace equation is linear and thus the principle of superposition is applicable; in other words, the magnetic field of a PM can be characterized by the sum of the magnetic fields contributed by an appropriate distribution of sources and sinks.

A. DMP Model of a Permanent Magnet (PM)

We define a *dipole* here as a pair of source and sink separated by a distance $\bar{\ell}$. A general DMP model with k loops (or columns) of n dipoles can be derived as follows. The potential $\Phi(x,y,z)$ at any point $P(x,y,z)$ contributed by all the dipoles (in terms of the ith dipole in the jth loop) is thus given by

$$\Phi=\sum_{j=0}^{k}\sum_{i=0}^{n}m_{ji}\varphi_{ji}=\underline{\varphi}^{\mathrm{T}}\underline{m} \tag{5}$$

where

$$\underline{\varphi}^{\mathrm{T}}=[(\varphi_{00}\cdots\varphi_{0n})\ \ (\varphi_{10}\cdots\varphi_{1n})\ \ (\cdots)\ \ (\varphi_{k0}\cdots\varphi_{kn})];$$
$$\underline{m}=[(m_{00}\cdots m_{0n})\ \ (m_{10}\cdots m_{1n})\ \ (\cdots)\ \ (m_{k0}\cdots m_{kn})]^{\mathrm{T}};$$
$$\varphi_{ji}=[(1/R_{ji+})-(1/R_{ji-})]/(4\pi)$$

where R_{ji+} and R_{ji-} expressed in terms of distance $\bar{\ell}$ are the distances from the source and sink to P, respectively, and m_{ji} is the strength of the jith dipole.

Similarly, since $\nabla(1/R)=-\mathbf{a}_R(1/R^2)$ where $\mathbf{a}_R=\mathbf{R}/R$, the magnetic flux density at P can be found from

$$\mathbf{B}=\sum_{j=0}^{k}\sum_{i=0}^{n}m_{ji}\boldsymbol{\beta}_{ji}=\underline{\boldsymbol{\beta}}^{\mathrm{T}}\underline{m} \tag{6}$$

where $\underline{\boldsymbol{\beta}}^{\mathrm{T}}=[(\boldsymbol{\beta}_{00}\cdots\boldsymbol{\beta}_{0n})\ (\boldsymbol{\beta}_{10}\cdots\boldsymbol{\beta}_{1n})\ (\cdots)\ (\boldsymbol{\beta}_{k0}\cdots\boldsymbol{\beta}_{kn})]$; and

$$\boldsymbol{\beta}_{ji}=-\frac{\mu_o}{4\pi}\left(\frac{\mathbf{a}_{Rji+}}{R_{ji+}^2}-\frac{\mathbf{a}_{Rji-}}{R_{ji-}^2}\right).$$

Note that (5) and (6) are in matrix form. For a DMP model that has a single dipole along the magnetization axis

$$\varphi_{j0}=\varphi_{0i}=\begin{cases}0 & i,j\neq 0\\ \varphi_0 & i=j=0\end{cases}$$

and

$$\beta_{j0}=\beta_{0i}=\begin{cases}0 & i,j\neq 0\\ \beta_0 & i=j=0.\end{cases}$$

The unknown parameters in (5) and (6) are $k,n,\bar{\ell}$, and m_{ji}.

For the purpose of deriving closed-form solutions to facilitate the design and control of PM-based devices, we seek the field solution outside the physical region of the magnet, particularly near its boundary. The problem is to find an appropriate distribution of dipoles to best approximate the field solution. To solve for the unknowns ($k, n, \overline{\ell}$, and m_{ji}), we minimize the error function (7) subject to constraints imposed by the magnet geometry and a limited set of known field solutions (as fitting points)

$$E = \int_z [\Phi(z) - \Phi_A(z)]^2 dz \tag{7}$$

where $\Phi_A(z)$ is a known solution derived analytically, or curve-fit from solved numerical solutions or measured experimental data along the magnetization axis (say, the z-axis). The general expression [11] of the magnetic scalar potential Φ_A created at $\mathbf{R}'(x', y', z')$ to the field point $\mathbf{R}(x, y, z)$ is given in

$$\Phi_A = \frac{1}{4\pi} \int_V \frac{-\nabla \cdot \mathbf{M}}{|\mathbf{R} - \mathbf{R}'|} dV + \frac{1}{4\pi} \int_S \frac{\mathbf{M} \cdot \mathbf{n}}{|\mathbf{R} - \mathbf{R}'|} dS \tag{8}$$

where $\mathbf{n}$ is the unit surface normal. The first integral in (8) is a volume integral over the body volume V, while the second one is a surface integral over the body boundary surface S. The corresponding magnetic flux density can be found using (2).

The constraints are formed from a set of specified points. For example, if the residual magnetic flux density of the magnet is specified (say at $z = z_o$), it can be used as a constraint

$$B(z_o) = B_A(z_o) = -\mu_o \nabla \Phi_A|_{z=z_o} \tag{9}$$

which can be expressed in terms of the dipoles using (6). Since (7) accounts for the potential field along the magnetization axis, the $(k \times n + 1)$ constraints include (9) and the potential along two other orthogonal directions from (5)

$$\begin{bmatrix} \underline{\beta}_0^T\big|_{z=z_o} \\ \underline{\varphi}_1^T \\ \vdots \\ \underline{\varphi}_{(k\times n)}^T \end{bmatrix} \underline{m} = \begin{pmatrix} B_A(z_o) \\ \Phi_{A1} \\ \vdots \\ \Phi_{A(k\times n)} \end{pmatrix}. \tag{10}$$

In (10), the subscript "0" denotes that the dipole is along the magnetization vector. If the known fields are in terms of the measured magnetic flux density, (6) instead of (5) can be used to obtain (10). For PM-based actuator applications, the $\mathbf{B}$ and Φ values in (10) are evaluated at an appropriate magnet surface. To avoid the singularity at $\mathbf{R} = \mathbf{R}'$, we choose

$$|\mathbf{R}| = \lim_{\varepsilon_R \to 0} (|\mathbf{R}'|\big|_{\substack{\text{point} \\ \text{at surface}}} + \varepsilon_R)$$

where ε_R is a small positive number. Three specific cases are worth mentioning.

i) If the relative permeability of the magnet is very large, the magnet surface can be approximated as equal potential, and Φ_{A} in (10) is a constant.

ii) If $\mathbf{M}$ is a constant implying $\nabla \cdot \mathbf{M} = 0$, the volume integral in (8) is zero and the potential field can be computed from the surface integral in (8).

iii) If the magnet is axisymmetric, the magnetic field is uniform in a particular direction (say θ). To minimize the field variation in the θ direction when modeling with a finite number of dipoles, the following constraint can be imposed:

$$\frac{\mathrm{Max}[\Phi(\theta)] - \mathrm{Mean}[\Phi(\theta)]}{\mathrm{Mean}[\Phi(\theta)]}\bigg|_{\text{at the edge}} \times 100\% \leqslant \varepsilon_\theta \tag{11}$$

where ε_θ is a specified (positive) error bound.

The DMP modeling method will be illustrated with examples in Sections III and IV. In general, the unknown parameters ($k, n, \overline{\ell}$, and m_{ji}) of a DMP model can be determined following the procedure summarized below.

Step 1) Compute Φ_{A} and $\mathbf{B}_{\mathrm{A}}$ analytically along the magnetization vector from (8) and (2), respectively.

Step 2) Generate an initial set of spatial grid points (k, n).

Step 3) Formulate (5) and (6) in terms of the unknowns, $\overline{\ell}$ and m_{ji}.

Step 4) Find $\overline{\ell}$ and m_{ji} by minimizing (7) subject to the constraint (10), where $\underline{\beta}^T$ and $\underline{\varphi}^T$ are obtained from (6) and (5), respectively. Error computed by (7) is saved.

Step 5) Check the condition (11). If (11) is not satisfied, increase k or n, and repeat from Step 3). Once (11) is met, the optimal parameters ($k, n, \overline{\ell}$, and m_{ji}) can be obtained by minimizing (7) using Step 4).

B. DMP Model of an Electromagnet (EM)

The magnetic field of a multilayer (ML) coil can be characterized by the DMP model by treating it as a PM. The process involves finding an equivalent single-layer (ESL) model. As will be shown, the ESL model greatly reduces computation of magnetic forces, while the DMP model offers a means to visualize the interacting magnetic fields between a PM and an EM. We derive here the effective radius and field density for the ESL coil (and the effective magnetization of the equivalent PM) to closely approximate the original ML coil.

Equivalent Single Layer (ESL) Model: For simplicity in illustrating the concept, we consider a typical multilayer (axisymmetrical) EM with a current density J. As shown in the sectional view in Fig. 2(a), the current flowing in the wire towards the $+x$-axis generates a circular magnetic flux. As a result, the cumulative magnetic flux parallel to the magnetization axis reverse its direction at some radial location $(a_i < y < a_o)$; this radial location is called the switching radius ρ and is a function of z. To find the switching radius (or the zero B_z-line of an axisymmetrical coil, where B_z is the z-component of $\mathbf{B}$), we consider the 2-D magnetic flux density of a single wire

$$\mathbf{B}(y_c, z_c) = \frac{\mu_0}{2\pi r}(\mathbf{I} \times \mathbf{e}_r) \tag{12}$$

where $\mathbf{I} = I\mathbf{e}_x$ and $I = \int_S J dS$. The total magnetic flux density at any point (with distance vector $\mathbf{R}$) can be calculated by integrating over the current-carrying conductor

$$\mathbf{B}(y, z) = \frac{\mu_0}{2\pi} \int_{-\ell/2}^{\ell/2} \left(\int_{a_i}^{a} \frac{|J|}{|\mathbf{R} - \mathbf{R}'|} + \int_{-a_i}^{-a_o} \frac{|J|}{|\mathbf{R} - \mathbf{R}'|} \right) dy' dz' \mathbf{e}_\theta \tag{13}$$

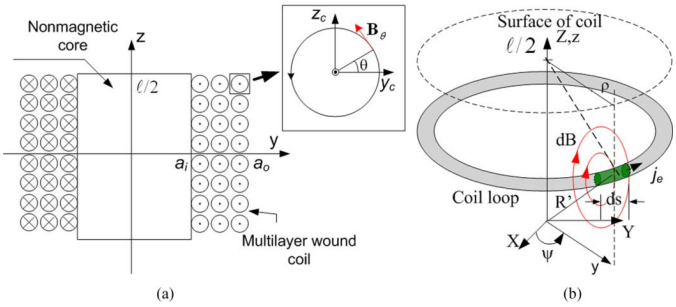

Fig. 2. Multilayer EM coil. (a) Cross sectional view. (b) Magnetic flux on the wire.

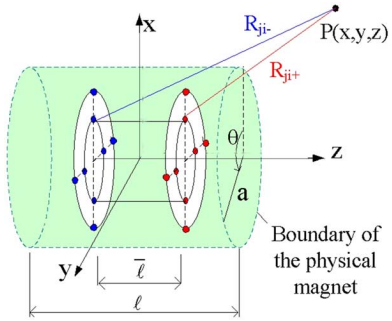

Fig. 3. DMP model of a cylindrical magnet.

and

$$\mathbf{e_\theta} = -\sin\theta \mathbf{e_y} + \cos\theta \mathbf{e_z}. \tag{13a}$$

The switching radius ρ satisfies the condition (14)

$$\mathbf{B}(\rho, z) \cdot \mathbf{e}_z = 0. \tag{14}$$

In general, the ESL model retains the shape of the original ML coil. For example, the ESL model of a cylindrical ML coil will have a constant radius computed from ρ at $z = \pm\ell/2$ and the corresponding effective current density can then be obtained from (15) at $y = 0$ and $z = \ell/2$.

The effective current density J_e is determined such that the magnetic flux densities of the original ML coil and the ESL model, $\mathbf{B}(y, z)$ and $\bar{\mathbf{B}}(y, z)$, respectively, have the same value at an appropriately specified location along the centroidal axis

$$[\mathbf{B}(y,z) = \bar{\mathbf{B}}(y,z)]_{\substack{\text{at the boundary} \\ \text{of the EM}}} \tag{15}$$

where

$$\frac{\bar{\mathbf{B}}(y,z)}{\mu_0 J_e d_w} = \frac{\mathbf{e}_\theta}{2\pi} \int_{-\ell/2}^{\ell/2} \left(\frac{1}{\sqrt{(y-\rho)^2 + (z-z')^2}} - \frac{1}{\sqrt{(y+\rho)^2 + (z-z')^2}} \right) dz' \tag{15a}$$

$$d_w = 2\sqrt{(a_o - a_i)\ell / N_c \pi} \tag{15b}$$

and N_c is the number of turns of the coil.

DMP Model of the Multilayer (ML) Coil: The ML coil can be modeled as a PM but its effective magnetization vector $\mathbf{M}$ is left to be determined from the effective current density J_e (15). With the aid of Fig. 2(b), the effective $\mathbf{M}$ can be found from (9), where the 3-D magnetic flux density is given by

$$\mathbf{B} = \frac{1}{4\pi} \int_{-\ell/2}^{\ell/2} \int_0^{2\pi} \frac{\mu_o J_e d_w}{|\mathbf{R} - \mathbf{R}'|^2} \mathbf{e}_\theta \rho \, d\psi \, dz' \tag{16}$$

where

$$|\mathbf{R} - \mathbf{R}'|^2 = (x - \rho\cos\psi)^2 + (y - \rho\sin\psi)^2 + (z - z')^2 \tag{16a}$$

and $\mathbf{e}_\theta$ is given in (13a). Once $\mathbf{M}$ is found for a specified magnetic flux density, the DMP model can be found following the procedure in Section II-A to characterize the EM.

General Procedure: The steps of finding the DMP model are as follows.

Step 1) Calculate the switching radius ρ that satisfies (14).

Step 2) Find the specific geometry of the equivalent single-layer EM and its effective current density J_e from (15).

Step 3) Model the EM as a PM that has the same geometry as the single-layer EM, the effective magnetization $\mathbf{M}$ is found using (9) and (16).

Step 4) The DMP model of the multilayer EM can then be derived using the procedure given in the previous section.

For an axisymmetrical EM, the 2-D models (12) and (13) can be used in Steps 1 and 2 to simplify calculations. However, the 3-D model (16) must be used to find the magnetization $\mathbf{M}$ in Step 3). Due to the symmetry, the tangential component of the flux along the centroidal axis is cancelled out automatically. A detailed example with model validation is given in the next section.

III. Cylindrical PM/EM and Model Validation

Cylindrical permanent magnets and electromagnets are commonly used, and some analytical solutions and/or experimental results are available for model validation. Thus, they are used here to illustrate the DMP modeling procedure. To facilitate practitioners in design, we express the formulas in dimensionless forms.

Example 1: Cylindrical Permanent Magnet: Consider a cylindrical magnet (radius a, length ℓ, and $\mathbf{M} = M_o \mathbf{e}_z$) as shown in Fig. 3. The potential and flux density field solutions along the z-axis are given in [11]

$$\frac{\Phi_A(Z)}{M_o \ell} = \frac{1}{4}\left[(A_- - |B_-|) - (A_+ - |B_+|)\right] \tag{17}$$

$$\frac{B_A(Z)}{\mu_o M_o} = \frac{1}{2}\left[\frac{|B_+|}{A_+} - \frac{|B_-|}{A_-} + c\right] \quad \text{where } c = \begin{cases} 0 & \text{if } |Z| \geqslant 1 \\ 2 & \text{if } |Z| < 1 \end{cases} \tag{18}$$

where $Z = 2z/\ell; \gamma = 2a/\ell; A_\pm = \sqrt{\gamma^2 + B_\pm^2}$ and $|B_\pm| = |Z \pm 1|$.

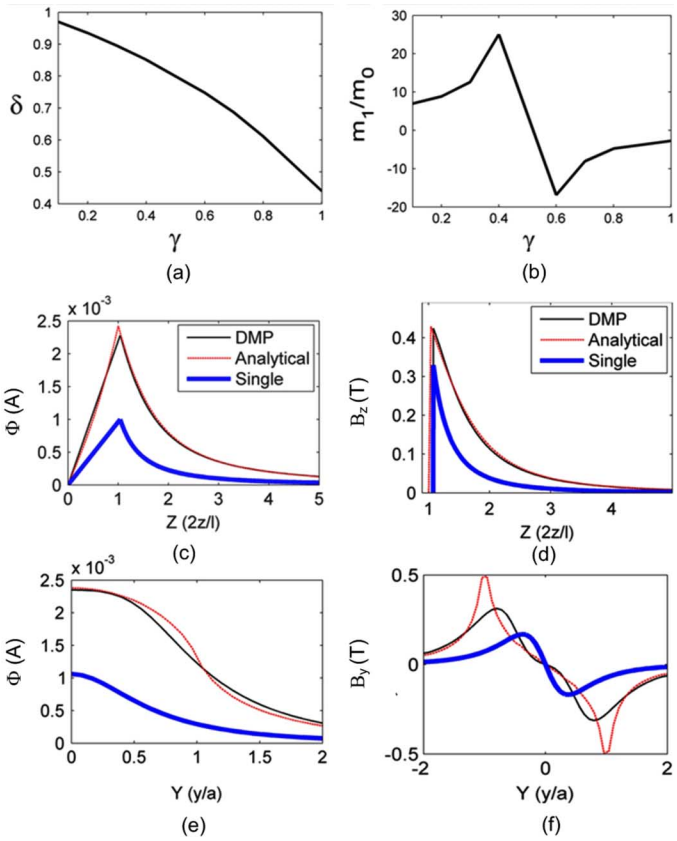

Fig. 4. Potential (in A) and flux density (in T) along the Y and Z axes. For all plots: $n = 4$ and $k = 1$; and for (c)–(f) $\gamma = 2a/\ell = 1$.

We model the PM using k circular loops of n dipoles parallel to the magnetization vector as shown in Fig. 3. The loops (each with radius $\bar{a}_j$) are uniformly spaced

$$\bar{a}_j = aj/(k+1) \text{ at } z = \pm\bar{\ell}/2 (0 \leqslant j \leqslant k) \tag{19}$$

$$0 < \bar{\ell} < \ell. \tag{20}$$

For a cylindrical magnet, the field is uniform circumferentially and hence $m_{ji} = m_j$. To minimize the field variation in the θ direction, we impose on n the constraint (11) evaluated at $r = a$ and $z = \ell/2$. The unknowns ($\bar{\ell}, m_j, n$, and k) are solved by minimizing (7) with $\Phi_{\rm A}$ and Φ given by (17) and (5), respectively, subject to the constraints imposed by (9), (10), (11), (19), and (20). For the DMP model shown in Fig. 3

$$R^2_{ji\pm} = [x - \bar{a}_j \cos i\theta_n]^2 + [y - \bar{a}_j \sin i\theta_n]^2 + (z \mp \bar{\ell}/2)^2 \tag{21a}$$

$$\frac{\mathbf{a}_{Rji\pm}}{R^2_{ji\pm}} = \frac{(x-\bar{a}_j \cos i\theta_n)\mathbf{a}_x + (y-\bar{a}_j \sin i\theta_n)\mathbf{a}_y + (z \mp \bar{\ell}/2)\mathbf{a}_z}{[(x-\bar{a}_j \cos i\theta_n)^2 + (y-\bar{a}_j \sin i\theta_n)^2 + (z \mp \bar{\ell}/2)^2]^{3/2}} \tag{21b}$$

where $i\theta_n$ indicates the angular position of the ith dipole on the jth loop and $\theta_n = 2\pi/n$.

To provide some insight and clarity in illustration, we derive and compare the following two cases.

Case A: Single Dipole Model: The simplest approximation is to model the field with a single dipole at $x = y = 0$, which

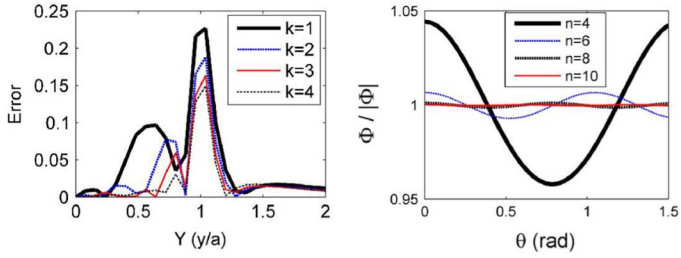

Fig. 5. Effect of n and k on modeling errors ($\gamma = 2a/\ell = 1$). (a) Effect of k on corner error. (b) Effect of n on variation in θ.

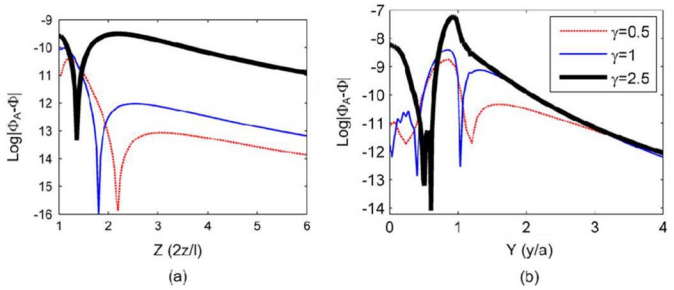

Fig. 6. Effect of the aspect ratio on modeling errors ($n = 4$). For $\gamma = 2a/\ell \leqslant 1, k = 1$; and for $\gamma = 2.5, k = 2$.

can be derived from (5)

$$\frac{\Phi(Z)}{(m/\ell)} = \frac{1}{2\pi}\left(\frac{1}{|Z-\delta|} - \frac{1}{|Z+\delta|}\right) \tag{22a}$$

and

$$\frac{\mathbf{B}(Z)}{\mu_o m/\ell^2} = \frac{4\delta Z}{\pi(Z^2-\delta^2)^2}\mathbf{a}_z \tag{22b}$$

where $\delta = \bar{\ell}/\ell$. However, as shown in (22a), (b) the single dipole model can not account for the shape of the PM (or more specifically, the aspect ratio γ of the cylindrical PM).

Case B: DMP Model ($\rm n = 4$)*:* To account for the shape

$$\frac{\Phi(Z)}{m_0/\ell} = \sum_{j=1}^{k} \frac{2m_j}{\pi m_0}\left(\frac{1}{\bar{A}_{j-}} - \frac{1}{\bar{A}_{j+}}\right) + \frac{1}{4\pi}\left(\frac{1}{|\bar{Z}_-|} - \frac{1}{|\bar{Z}_+|}\right) \tag{23a}$$

$$\frac{\mathbf{B}(Z)}{\mu_o m_o/\ell^2} = \frac{1}{\pi}\sum_{j=1}^{k}\frac{m_j}{m_o}\left[\frac{\bar{Z}_-}{\bar{A}^3_{j-}} - \frac{\bar{Z}_+}{\bar{A}^3_{j+}}\right] + \left(\frac{1}{\bar{Z}^2_- - \bar{Z}^2_+}\right) \tag{23b}$$

where $\bar{A}_{j\mp} = \sqrt{\bar{\gamma}_j^2 + (\bar{Z}_\mp)^2}$; $\bar{Z}_\mp = Z \mp \delta$; and $\bar{\gamma}_j = 2\bar{a}_j/\ell$.

The results are given in Figs. 4–6, and Table I where

$$\%\text{Error} = 100 \times \int_z |\Phi(z) - \Phi_A(z)|dz \Big/ \int_z |\Phi_A(z)|dz.$$

Results in Table I were computed using MATLAB Optimization Toolbox. Since (8) is singular at the surface of a magnet, the Φ_A values for (10) are solved numerically with $|\mathbf{R}'| + 10^{-6}$; no significant difference in results was found when $\varepsilon_R \leqslant 10^{-3}$.

Some other observations are discussed as follows.

TABLE I
VALUES OF THE PARAMETERS IN EXAMPLE 1

Model	$\delta = \bar{\ell}/\ell$	m (A·m)	%Error
Single (n= k=0)	0.20	206.91	55.49
DMP (n=4,k=1)	0.39	m_o=-33.31; m_{1i}=78.13	1.76

$\mu_0 M_0 = 1$T , $\ell = 12.7$ mm , $\varepsilon_R = 10^{-6}$.

1) For a given aspect ratio $\gamma = 2a/\ell$, the parameters, $\delta = \bar{\ell}/\ell$ and m_j/m_o, can be calculated. The results for $\gamma \leqslant 1$ (with $k = 1$ and $n = 4$) are given in Fig. 4(a) and (b). Once k, n, δ, and m_j/m_o are known, m_o can be determined for a specified B_r from (23b). In Fig. 4(a), δ decreases as γ increases as expected. For a given δ, the curve m_1/m_o in Fig. 4(b) depends only on the first term of (23a) or (23b). Fig. 4(b) also shows that the case $m_1/m_o = 0$ (or only a single dipole) is very limited.
2) The DMP model is compared against the single dipole model and analytical solution in Fig. 4(c)–(f). The analytical solution agrees well with the DMP model that uses only five dipoles ($n = 4$ and $k = 1$) to characterize the potential field and flux density of a PM with a unity aspect ratio ($\gamma = 1$). The single dipole, on the other hand, only provides a reasonable estimate of the magnetic flux density along the z-axis.
3) The discrepancy in Fig. 4(f) occurs primarily around the corner ($r = a, z = \ell/2$) of the PM; the errors in the magnetic flux density can be reduced by using more loops k. Fig. 5 illustrates the effects of n and k on modeling accuracy.
4) Fig. 5(b) shows the effect of increasing n in the circular loop, which effectively improves the uniformity circumferentially. The variation is about 5% with only five dipoles ($n = 4$ and $k = 1$), and nearly eliminated with $n \geqslant 6$.
5) As shown in Fig. 6(a) and (b), where the absolute differences between the analytical and DMP modeled potentials are graphed in $\log_{10}$ scale, the model (with an increase in k) can be extended to account for the effect of larger aspect ratios.

Example 2: Cylindrical Electromagnet (EM): The geometry (a_o, a_i, ℓ) of the cylindrical ML coil considered here is defined in Fig. 2(a). We derive the ESL model (and DMP model) that has a radius defined by

$$[\mathbf{B}(\rho, Z) \cdot \mathbf{e}_z]_{Z=z/(\ell/2)=1} = 0. \tag{24}$$

In addition, we validate the model by comparing three different methods for calculating the magnetic forces against data obtained experimentally and numerically.

Switching Radius: The switching radius ρ can be analytically derived by substituting (13) into (14); the current density $J = N_c I/[(a_o - a_i)\ell]$ drops out. In normalized form

$$\int_{-1}^{1} \left(\int_{\gamma_i'}^{\gamma_o'} \frac{\gamma' - Y'}{\sqrt{(\gamma' - Y')^2 + (Z - Z')^2}} + \int_{-\gamma_i'}^{-\gamma_o'} \frac{\gamma' - Y'}{\sqrt{(\gamma' - Y')^2 + (Z - Z')^2}} \right) dY' dZ' = 0$$

which can be written as

$$\alpha_+(\gamma') + \alpha_-(\gamma') + \beta_{i-}(\gamma') - \beta_{0-}(\gamma') + \beta_{i+}(\gamma') - \beta_{o-}(\gamma') = 0 \tag{25}$$

where

$$\alpha_\pm(\gamma') = (1 \pm Z)\ell og \left\{ \left[\frac{(\gamma' - \gamma_i')^2 + (1 \pm Z)^2}{(\gamma' - \gamma_o')^2 + (1 \pm Z)^2} \right] \times \left[\frac{(\gamma' + \gamma_i')^2 + (1 \pm Z)^2}{(\gamma' + \gamma_o')^2 + (1 \pm Z)^2} \right] \right\};$$

$$\beta_{i\pm}(\gamma') = 2(\gamma' \pm \gamma_i') \tan^{-1} \left[\frac{2(\gamma' \pm \gamma_i')}{(\gamma' \pm \gamma_i')^2 - (1 - Z^2)} \right];$$

$$\beta_{o\pm}(\gamma') = 2(\gamma' \pm \gamma_o') \tan^{-1} \left[\frac{2(\gamma' \pm \gamma_o')}{(\gamma' \pm \gamma_o')^2 - (1 - Z^2)} \right];$$

$Y' = 2y'/\ell, Z' = 2z'/\ell; \gamma_o' = 2a_o/\ell; \gamma_i' = 2a_i/\ell$ and $\gamma' = 2\rho/\ell$. The normalized switching radius γ' can be solved as a function of Z from (25).

Effective Field Intensity: Since the flux density is symmetrical and maximum at $(Y = 0, Z = 1)$, the effective current density J_e is determined such that $|\mathbf{B}(0,1)| = |\bar{\mathbf{B}}(0,1)|$, where $\mathbf{B}$ and $\bar{\mathbf{B}}$ are the flux density of the ML coil and that of the ESL model, respectively.

The magnetic flux density of the ESL model can be obtained from (15a). In closed form

$$\frac{\bar{\mathbf{B}}(Y,Z)}{\mu_0 J_e d_w} = \frac{\mathbf{e}_\theta}{2\pi} \ell og \frac{(Z_+ + \sqrt{Z_+^2 + Y_+^2})(Z_- + \sqrt{Z_-^2 + Y_-^2})}{(Z_+ + \sqrt{Z_+^2 + Y_-^2})(Z_- + \sqrt{Z_-^2 + Y_+^2})} \tag{26}$$

where in short, we write $Z_\pm = Z \pm 1$ and $Y_\pm = Y \pm \gamma'$. Equating $|\bar{\mathbf{B}}(0,1)|$ from (26) to $|\mathbf{B}(0,1)|$ from (13), the effective field intensity is given by

$$J_e d_w = \frac{\pi}{\mu_0} |\mathbf{B}(0,1)| \ell og[(1 + \sqrt{1 + (\gamma'/2)^2})/(\gamma'/2)]. \tag{27}$$

Once the ESL model is found, it can be further characterized by an equivalent PM with the same radius (ρ calculated at $z = \ell/2$) and length ℓ. The magnetic flux density $\mathbf{B}(0,0,1)$ can be found from (2) and (8)

$$\mathbf{B}(0,0,1) = \frac{\mu_o J_e d_w \rho}{2\pi} \left(\frac{2}{\ell} \right)^{4/3} \int_{-1}^{1} \frac{(1 - Z)}{[\gamma'^2 + (1 - Z)^2]^{3/2}} dZ. \tag{28}$$

Finally, we have from (9) and (28)

$$M_o = 2\mathbf{B}(0,0,1)\sqrt{(\gamma/2)^2 + 1}/\mu_o. \tag{29}$$

Numerical Example: To illustrate the method and validate the DMP models, we model the setup (with two different size combinations) as shown in Fig. 7, and compare the computed forces against numerical solutions [12] and published experimental data [13]. As an illustration, Fig. 8(a) shows the normalized switching radius as a function of Z for the larger coil, where the effective radius is defined at $Z = 1$. Table II lists the calculated effective radii and field intensity of the ESL models, and the corresponding parameters of the DMP models.

Fig. 8(b) compares the three different methods for calculating the corresponding magnetic flux density along the z-axis;

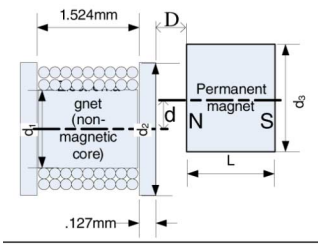

Size	Large	Small
d_1 (mm)	3.048	1.524
d_2 (mm)	3.962	3.175
d_3 (mm)	2.998	1.6
L (mm)	1.6	0.813
Coil res. (Ω)	57	32
Wire length (m)	3	1.68

Samarium-Cobalt magnet; $\mu_0 M_0$=1.02 T
Coil: 280 turns of #47 wire; Current=0.05A

Fig. 7. Experimental setup and parameters.

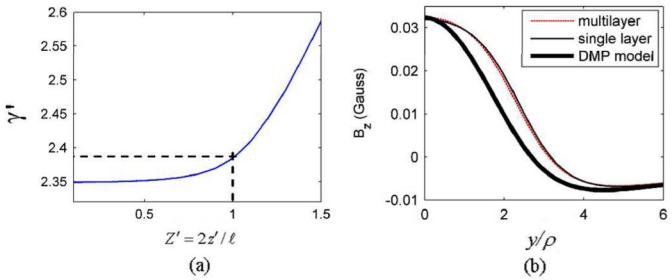

Fig. 8. Switching radius and B_z for the large coil ($\gamma_i' = 2, \gamma_o' = 2.5984$). (a) Switching radius (large coil). (b) B_z at ($\ell/2 + 1$ mm).

TABLE II
PARAMETERS OF THE EQUIVALENT MODELS

	Parameters	Large	Small
PM (DMP)	δ	0.3140	0.3122
(k=2; n=6)	m_j (μA·m)*	1.65, 0.02, 3.80	0.43, 0.02, 1.07
EM	ρ (mm)	1.8168	1.456
(Single-layer)	$J_e d_w$ (A/m)	2.2750 e-5	3.8975 e-5
EM(DMP)	δ	0.3833	0.56
(k=2; n=6)	m_j (nA·m)	11.31, 2.59, 38.80	7.5, 1.3, 21.2

*m_j, j=1, 2, 3.

namely, the original ML coil (13), the ESL model (26), and the DMP model of the EM. The comparisons are remarkably close.

Model Validation With Force Computation: The magnetic forces (between a PM and an EM in Fig. 7) were computed using the three different EM models: (i) original ML coil; (ii) ESL model; and (iii) equivalent PM (DMP model). Models (i) and (ii) use the *Lorentz force equation* (A.1) to calculate the magnetic force exerted on the current-carry conductors of the ML and the ESL coils, respectively. Model (iii) treats the EM as a PM, and uses *Maxwell stress tensor* (A.3) to calculate the force on the given field of the effective PM. Both the Lorentz force equation and the Maxwell stress tensor are given in the Appendix. The modeled axial and tangential forces are compared in Fig. 9(a), (b), and (c), (d), respectively, against published experimental data and numerical results computed using the meshless method (MLM) [12].

As shown in Fig. 9, both the Lorentz-force computation models (the original ML coil and its ESL model) very closely agree with each other and with the MLM one. Maximum differences from the experimental data, $100 \times |F_m - F_{\exp}|/|F_{\exp}|$, are within 10% as shown in Table III. As compared in Fig. 9, the force prediction using the DMP model with Maxwell stress tensor is as good as the experimental data.

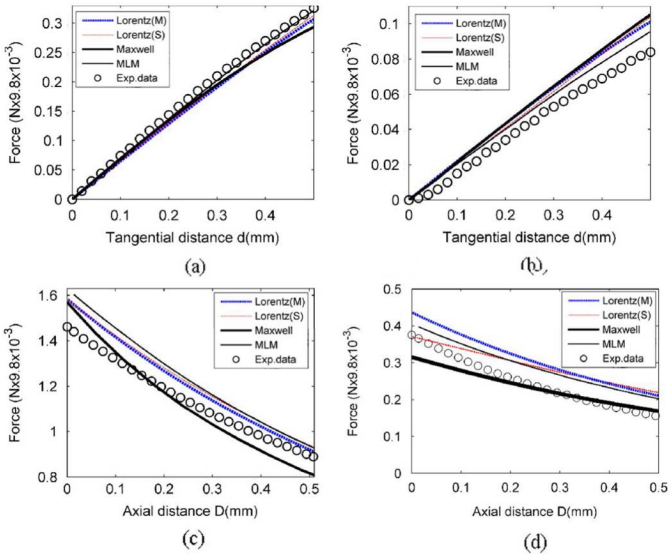

Fig. 9. Comparisons between computed and experimental results. (a) Tangential forces (large). (b) Tangential forces (small). (c) Axial forces (large). (d) Axial forces (small).

TABLE III
MAXIMUM DIFFERENCES FROM PUBLISHED EXPERIMENTAL DATA

	Lorentz force equation (A.1)		Maxwell tensor (A.3)
	Multilayer	Single layer	Equivalent PM
Tangential	5.79 %	3.57 %	8.92 %
Axial	8.21 %	8.14 %	9.04 %

IV. ILLUSTRATIVE APPLICATIONS

We illustrate two examples here. The first extends the DMP modeling method to characterize PM of customized shape. The second investigates the effect of three different pole shapes on the magnetic torque using DMP models.

Example 3: Permanent Magnet of Customized Shape: Fig. 10 shows an example of customized PM used in a prototype spherical motor [4] where the magnet (shaped as a segment of a sphere) was magnetized in the positive x-axis. The potential field solution can be derived analytically from (8). Since $\mathbf{M} = M_o \mathbf{e}_x$ implying $\nabla \cdot \mathbf{M} = 0$, the volume integral in (8) is zero. With the differential surface and unit normal for each of the surfaces given in Table IV where spherical coordinates (r, θ, ϕ) are defined in Fig. 1, the potential field can be computed from the surface integral in (8).

As shown in Fig. 10, the dipoles of the DMP model for the customized PM are uniformly located in a $\bar{r}_1 \times \bar{r}_2$ region where $r_o > \bar{r}_1 > \bar{r}_2 > r_i$ such that they form a $k \times n$ lattice as defined in Fig. 10(b) and (c). Their locations are given by

$$\phi_{2\mathrm{j}} = j\phi_o/(k+1); \tag{30a}$$

$$\theta_{2\mathrm{i}} = i\theta_o/(n+1). \tag{30b}$$

Since the dipoles are parallel to the x-axis, from Fig. 10(c) we have $\bar{r}_1 \cos\phi_{1\mathrm{j}} = \bar{r}_2 \cos\phi_{2\mathrm{j}}$ or

$$\phi_{1\mathrm{j}} = \cos^{-1}(\bar{r}_2 \cos\phi_{2\mathrm{j}}/\bar{r}_1). \tag{31a}$$

Similarly, from the projections on the x-axis in Fig. 10(b)

$$\theta_{1\mathrm{i}} = \sin^{-1}\left[\frac{\bar{r}_2 \sin\phi_{2\mathrm{j}}}{\bar{r}_1 \sin\phi_{1\mathrm{j}}} \sin\theta_{2\mathrm{i}}\right]. \tag{31b}$$

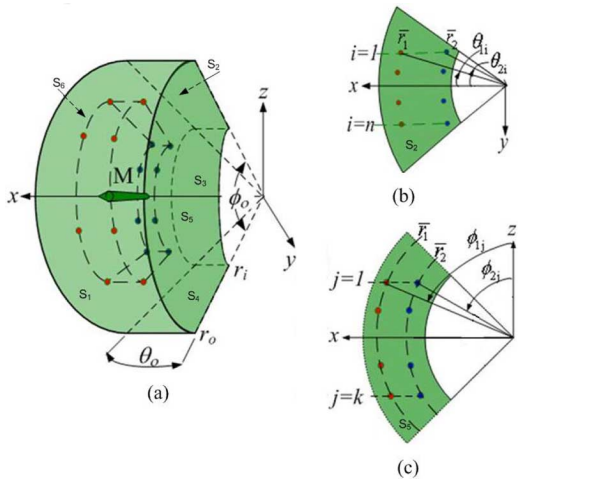

Fig. 10. Customized PM geometry ($r_o = 46.5$ mm, $r_i = 23$ mm, $\theta_o = 40°, \phi_o = 70°; \mu_o M_o = 0.62$ T). (a), (b) $n = 5$, (c) $k = 11$.

TABLE IV
PARAMETERS FOR SURFACE INTEGRAL (8)

Surfaces	Differential	Surface normal
$r=r_o$ $r=r_i$	$dS_{1,3} = r_{o,i}^2 \sin\phi\, d\theta\, d\phi$	$\hat{n}_1 = -\hat{n}_3 = \mathbf{e}_r = \sin\phi\cos\theta\mathbf{e}_x + \sin\phi\sin\theta\mathbf{e}_y + \cos\phi\mathbf{e}_z$
$\phi=\phi_2$, $\phi=\phi_4$	$dS_{2,4} = r dr d\theta$	$\hat{n}_2 = -\sin\phi_1\mathbf{e}_x + \cos\phi_1\mathbf{e}_z$ $\hat{n}_4 = -\sin\phi_2\mathbf{e}_x - \cos\phi_2\mathbf{e}_z$
$\theta=\theta_5$, $\theta=\theta_6$	$dS_{5,6} = r\sin\phi\, dr d\phi$	$\hat{n}_5 = -\sin\theta_1\mathbf{e}_x + \cos\theta_1\mathbf{e}_y$ $\hat{n}_6 = \sin\theta_2\mathbf{e}_x - \cos\theta_2\mathbf{e}_y$

TABLE V
PARAMETERS OF THE 11 × 5 DMP MODEL (m_{ji}, WHERE $j = 1, \ldots, 6$)

i=1	7.0594	-0.0453	4.1249	2.0897	3.2027	2.5187
i=2	-0.9223	-1.0204	-0.1404	-0.7011	-0.2487	-0.5497
i=3	1.7825	0.3004	1.0298	0.6462	0.8940	0.7231

δ_1=0.3951; δ_2=0.1702

Since the magnet is symmetric about xy and xz planes, only one quarter of the dipole moments m_{ji} are found numerically using the optimization toolbox in MATLAB. The values are given in Table V. To allow for one more degree of freedom to describe the location of the dipoles, we define the source-sink spacing using two variables:

$$\delta_1 = \frac{\bar{r}_1 - r_c}{r_o - r_c} \quad \text{and} \quad \delta_2 = \frac{\bar{r}_2 - r_c}{r_o - r_c}; \quad \text{where } r_c = \frac{r_o + r_i}{2}. \tag{32}$$

The customized magnet was studied experimentally in [4] and [14] giving measured magnetic flux density along the x-axis, and the ϕ direction in the y–z plane. These data are used here as a basis for comparison. We compute the flux density of the customized magnet using three different models, and compare the computed results against published data in Fig. 11.

i) *Analytical integral* (8) with $\mathbf{M} = M_o\mathbf{e}_x$ and Table IV.
ii) *Analytical integral (r-only)*: same as (i) but neglects ϕ and θ components of the magnetization; this model assumes a uniform radial field $\mathbf{M} \approx M_o \cos\theta \sin\phi \mathbf{e}_r$ [4].
iii) 11 × 5 *DMP model* (Table V) and $\mathbf{M} = M_o\mathbf{e}_x$ as in (i).

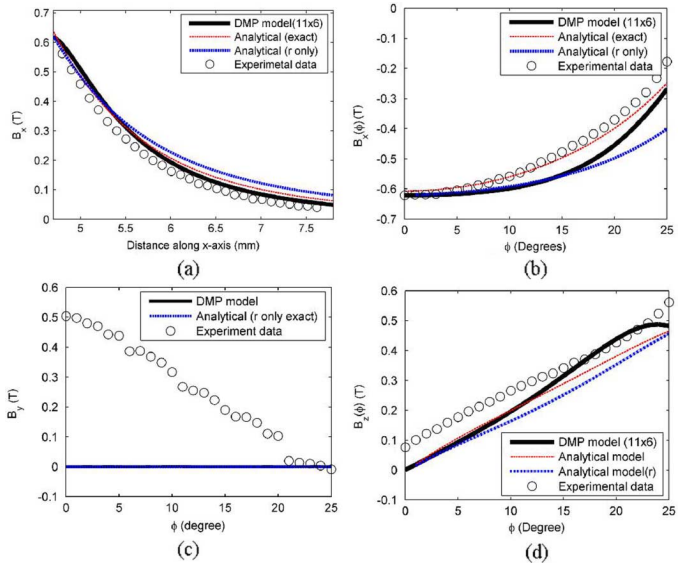

Fig. 11. Comparisons of magnetic flux density. (a) x-axis, (b) $\mathrm{B_x}(\phi)$, (c) $\mathrm{B_y}(\phi)$, (d) $\mathrm{B_z}(\phi)$.

Some observations from the comparisons are summarized.

- As shown in Fig. 11(a), the computed $B_x(x, 0, 0)$ of the DMP model along the x-axis closely agrees with both the analytical solution and experimental data. Note that since $\mathbf{M} = M_o\mathbf{e}_x, B_y = B_z = 0$ along the x-axis.
- The three components of $\mathbf{B}$ that were measured at locations ($r = r_o + 0.5$ mm, $\theta = 0$) in terms of ϕ are given in Fig. 11(b)–(d). The DMP computed B_x and the results of the first analytical integral agree well with the measured B_x data.
- $B_y(\phi)$ and $B_z(\phi)$ of the DMP model lie between the analytical integral model and the experimental data. Some discrepancies are observed between the computed and measured $B_y(\phi)$ and $B_z(\phi)$, which may be explained as follows. Since Φ is symmetric about the y–z plane, analytically we should have

$$B_y = -\mu_0[\partial\Phi/\partial y]_{y=0} = 0 \quad \text{and} \quad B_z|_{y=z=0} = 0.$$

However, measured B_y in Fig. 10(c) and B_z at $y = z = 0$ in Fig. 10(d) are not zero, suggesting that the customized PM may not uniformly magnetized or that there could be some systematic errors in measured $B_y(\phi)$ and $B_z(\phi)$.

Example 4: Effect of Pole Shape and Design Configuration: The geometry and layout of the PMs have a significant influence on the magnetic torque of a PM-based actuator. This example illustrates the use of DMP models to investigate the effect of pole shapes on the magnetic torque of a spherical motor. The PM pole shapes used in the following designs are considered:

Design A [15] consists of two rows of eight cylindrical PMs ($\gamma = 1$).
Design B [16] uses a row of eight assemblies of five cylindrical PMs with $\gamma > 1$.
Design C [4] is similar to *Design B* but the customized PMs (Fig. 10) are used as rotor poles.

We focus on comparing the net magnetic torque per unit magnet-volume for a given rotor radius and under the same

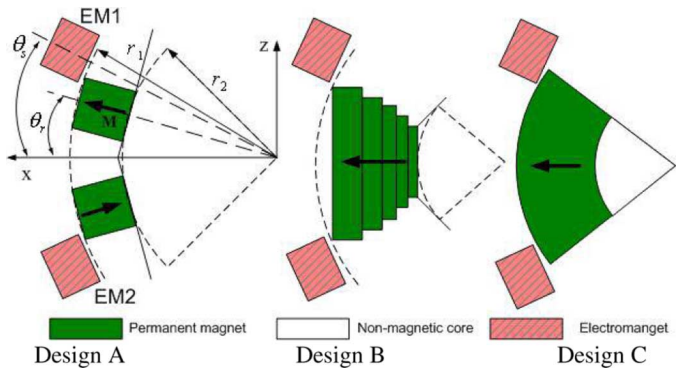

Fig. 12. PM pole shape designs.

TABLE VI
PARAMETERS USED IN SIMULATION

Common Parameters				
Rotor radius, mm	**Stator EM ($2\theta_s$=26°)** $(2a_o)\times(2a_i)\times\ell$ **(mm)***	**# of turns**	**Current (A)**	**Air gap mm**
r_i=37.5	19.05×9.53×25.4	1050	±1	0.5

PM Pole Designs			
	$\mu_0 M_0$ (T)	**PM pole shape (mm)**	**Volume (cm^3)**
Design A	1.27	$2a=\ell=12.7$, $2\theta_i$=20°	3.22
Design B	1.27	$2a\times\ell$: 25×10, 20×5, 16×6, 12×3, 8×3	8.2
Design C	0.62	Fig. 10 (r_o=46.5, r_i=23, ϕ_o=70°, θ_o=40°)	23.6

influence of the stator electromagnets. Detailed geometries of the three PM pole shapes are compared in Fig. 12, where the **bold arrow** indicates the polarity of the PM. The parameters used in simulation are summarized in Table VI.

Simulated magnetic flux and potential lines are plotted in Fig. 13; as expected, the potential and flux lines are orthogonal. Fig. 13(a), or the left column, compares the magnetic fields of the three different PM designs. Unlike *Designs B* and *C* where only one row of PMs is used, a significant portion of the flux lines in *Design A* forms a closed path between two PMs. Once the magnetic field of the PMs is found, the force acting on the current-carrying conductors can be calculated using the Lorentz force (A.1). Fig. 14 compares the torque per unit volume of the three designs. The calculation in Fig. 14 uses the ESL model with the magnetic field given in Fig. 13(a). In calculating the torques, ±1 A current profiles in Figs. 14(a) and (b) are given to the EMs such that a positive torque in +y-direction is generated.

Fig. 14(c) shows that *Design A* offers the largest electromagnetic energy to mechanical energy (area under the torque-displacement curve) conversion, and that *Design C* has the smallest torque-to-volume ratio. These observations can be explained by comparing the magnetic fields of the designs. As an illustration, snapshots of the combined (PM and EM) fields for the three designs are compared in Fig. 13(b), where ±1 Ampere of current is given to the pair of EMs such that a magnetic torque is generated in +y-direction. In other words, the upper EM is repulsive while the lower EM is attractive. The comparison shows that *Design A* has significantly less leakage fluxes in the attractive PM or EM, and less attractive fluxes in the repulsive EM than *Designs B* and *C*. The leakage fluxes in the attractive PM

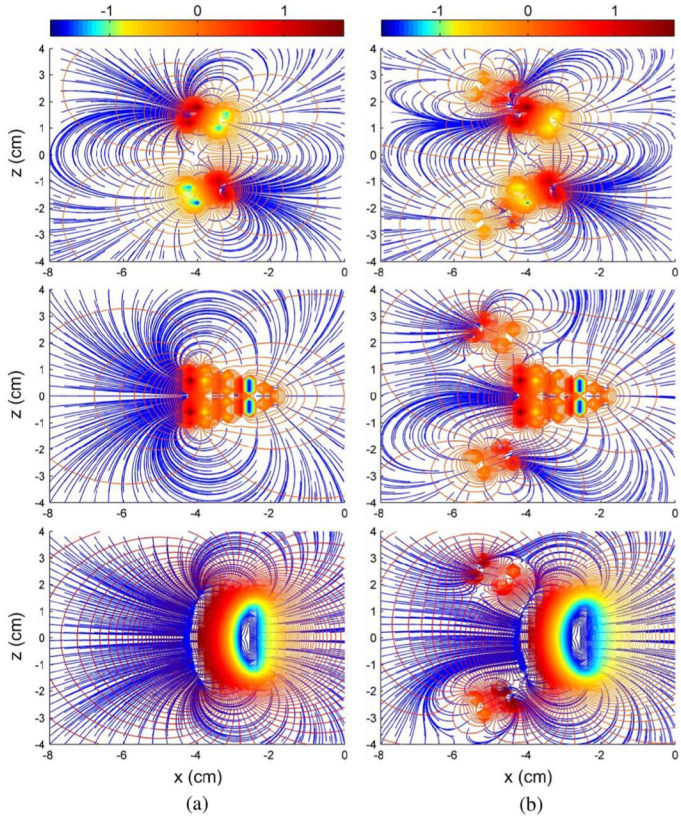

Fig. 13. Magnetic fields (Orange line: potential; blue lines: magnetic flux) Top: Design A; middle: Design B; bottom: Design C. (a) PM only. (b) Combined PM and EM (±1 A).

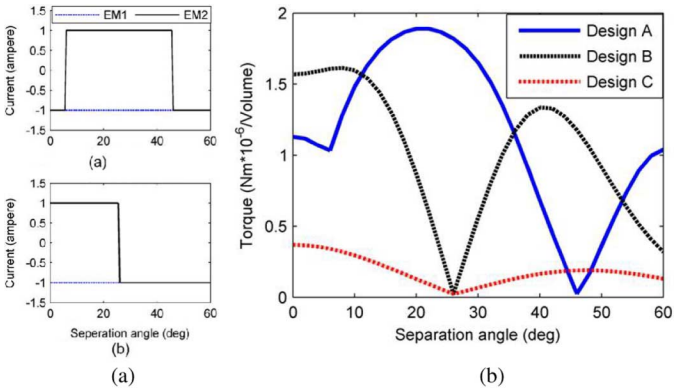

Fig. 14. Comparison of torque/volume. (a) Current input. (b) Torque comparison.

or EM are considered losses as they do not contributes to mechanical torques. Due to the large exposed surfaces in *Designs B* and *C*, a relatively strong closed path of magnetic flux is formed between the repulsive EM and the single PM, which would produce an opposing torque, and thus reduce the net torque. In addition, significantly large leakage fluxes from the customized magnet (region between the two EMs) can be seen in *Design C* indicating PM is oversized for the specified EMs. As illustrated in Fig. 13(b), the closed-form solution of the DMP models can offer an inexpensive means to visualize and analyze the effect of the EM fields on the leakage and unexpected flux paths that have significant influences on the magnetic torque.

V. Conclusion

A general DMP modeling method which derives a closed-form solution for calculating the magnetic field of a permanent magnet or an electromagnet has been presented. This method, which extends the concept of a magnetic doublet beyond the context of physics, provides an effective means to account for the shape and magnetization of the physical magnet.

A relatively complete DMP model has been derived for general cylindrical magnets with axial magnetization, and validated by comparing computed results against published experimental and numerical data. In the process of obtaining a DMP model for a multilayer electromagnet, we derive an equivalent single-layer model that significantly reduces the computational effort for calculating the magnetic force.

The simplicity of the closed-form solution, along with precise (and yet intuitive) magnetic fields of the DMP models, has been demonstrated with four practical examples. The advantage of being able to offer an inexpensive means to visualize the magnetic fields will make the DMP modeling method an attractive alternative to the existing (analytic, numerical, and lumped-parameter) methods for actuator design. We expect that the DMP modeling method presented here provides a basis for other magnetic field calculations; see for example [17], where a dipole approximation has been proposed for calculating magnetic fields involving nonlinear iron boundaries.

Appendix

The magnetic force in static magnetic fields can be computed by the following two methods: Lorentz force equation or Maxwell stress tensor.

The **Lorentz force** equation is commonly used to calculate the magnetic force exerted on current-carrying conductors. Since the current vector directly used in the known field, it is not necessary to compute the magnetic flux generated by the current loop

$$\mathbf{F} = -\oint \mathbf{B} \times I d\mathbf{L} \quad \text{where } I = \iint \mathbf{J} \cdot d\mathbf{S} \tag{A.1}$$

where $\mathbf{L}$ is normalized current direction vector.

Alternatively, the magnetic force can be derived using the principle of virtual displacement

$$\mathbf{F} = \nabla W_m \quad \text{where } W_m = \frac{1}{2} \int_V \mathbf{H} \cdot \mathbf{B} dv' \tag{A.2}$$

where the volume V is taken to be sufficiently large to contain the magnetic field involved. Equation (A.2) is written in term of **Maxwell stress tensor T**

$$\mathbf{F} = \oint_\Gamma \mathbf{T} d\Gamma \quad \text{where } \mathbf{T} = \frac{1}{\mu_0} \left(\mathbf{B}(\mathbf{B} \cdot \mathbf{n}) - \frac{1}{2} B^2 \mathbf{n} \right) \tag{A.3}$$

where Γ is an arbitrary boundary enclosing the body of interest; and $\mathbf{n}$ is the normal of the boundary interface. Equation (A.3) computes the force on the given field. Once $\mathbf{B}$ is known, the force on a body can be computed from the surface integration.

Acknowledgment

This work was jointly supported by the Georgia Agricultural Technology Research Program (ATRP) and the U.S. Poultry and Eggs Association.

References

[1] K.-M. Lee and C. Kwan, "Design concept development of a spherical stepper for robotic applications," *IEEE Trans. Robot. Autom.*, vol. 7, no. 1, pp. 175–181, Feb. 1991.

[2] R. L. Hollis, S. E. Salcudean, and A. P. Allan, "A six-degree-of-freedom magnetically levitated variable compliance fine-motion wrist: Design, modeling, and control," *IEEE Trans. Robot. Autom.*, vol. 17, no. 3, pp. 320–332, Jun. 1991.

[3] J. Wang, G. Jewell, and D. Howe, "Design and control of a novel spherical permanent magnet acutator with three degrees of freedom," *IEEE/ASME Trans. Mechatronics*, vol. 8, no. 4, pp. 457–468, Dec. 2003.

[4] Y. Liang, I. M. Chen, G. Yang, L. Wei, and K.-M. Lee, "Analytical and experimental investigation on the magnetic field and torque of a permanent magnet spherical actuator," *IEEE/ASME Trans. Mechatronics*, vol. 11, no. 4, pp. 409–419, Aug. 2006.

[5] K.-M. Lee, R. A. Sosseh, and Z. Wei, "Effects of the torque model on the control of a VR spherical motor," *IFAC J. Control Eng. Practice*, vol. 12, pp. 1437–1449, 2004.

[6] D. J. Craik, "Magnetostatics of axially symmetric structure," *J. Phys.*, vol. 7, p. 1566, 1974.

[7] M. A. Green, "Modeling the behavior of oriented permanent magnet material using current doublet theory," *IEEE Trans. Magn.*, vol. 24, no. 2, pp. 1528–1531, Mar. 1988.

[8] W. S. Bennett, "Basic sources of electric and magnetic fields newly examined," *IEEE Antennas Propag. Mag.*, vol. 43, no. 1, pp. 31–35, Feb. 2001.

[9] S. Nedelcu and J. H. P. Watson, "Mangetic dipole model of a permanent magnet based device," *J. Phys.*, vol. 34, no. 17, pp. 2622–2628, 2001.

[10] P. De Visschere, "An exact two-dimensional model for a periodic circular array of head-to-head permanent magnets," *J. Phys. D: Appl. Phys.*, vol. 38, no. 3, pp. 355–362, 2005.

[11] J. D. Jackson, *Classical Electrodynamics*. New York: Wiley, 1999.

[12] Q. Li and K.-M. Lee, "An adaptive meshless method for magnetic field computation," *IEEE Trans. Magn.*, vol. 42, no. 8, pp. 1996–2003, Aug. 2006.

[13] N. I. J. P. A. Bastos, "Forces in Permanent Magnets Team Workshop Problem 23," [Online]. Available: http://www.compumag.co.uk/team.html

[14] Y. Liang, "Modeling and design of a three degree-of-freedom permanent magnet spherical actuator," Ph.D. thesis, Nanyang Technological University, Singapore, 2005.

[15] K.-M. Lee and H. Son, "Torque model for design and control of a spherical wheel motor," in *Proc. IEEE/ASME AIM*, 2005, pp. 335–340.

[16] Y. Liang, I.-M. Chen, C. K. Lim, G. Yang, W. Lin, and K.-M. Lee, "Experimental investigation on the magnetic field of a permanent magnet spherical actuator," in *Proc. IEEE/ASME AIM*, 2005, pp. 347–352.

[17] B. Krevet, "Nonlinear magnetic field calculation using dipole approximation," *IEEE Trans. Magn.*, vol. 28, no. 2, pp. 1060–1063, Mar. 1992.

Manuscript received August 30, 2006; revised July 18, 2007. Corresponding author: K. Lee (e-mail: kokmeng.lee@me.gatech.edu).